Journal of
Marine Science and Engineering

MDPI

Article

Simulation-Driven Design Optimization of a Destroyer-Type Vessel via Multi-Fidelity Supervised Active Learning

Emanuele Spinosa [1], Riccardo Pellegrini [1], Antonio Posa [1], Riccardo Broglia [1], Mario De Biase [2] and Andrea Serani [1,*]

[1] CNR-INM, National Research Council-Institute of Marine Engineering, 00128 Rome, Italy; emanuele.spinosa@inm.cnr.it (E.S.); riccardo.pellegrini@cnr.it (R.P.); antonio.posa@cnr.it (A.P.); riccardo.broglia@cnr.it (R.B.)
[2] CEIMM, Italian Navy Hydrodynamic Research Center, 00128 Rome, Italy; mario.debiase@marina.difesa.it
* Correspondence: andrea.serani@cnr.it

Abstract: The paper presents the use of a supervised active learning approach for the solution of a simulation-driven design optimization (SDDO) problem, pertaining to the resistance reduction of a destroyer-type vessel in calm water. The optimization is formulated as a single-objective, single-point problem with both geometrical and operational constraints. The latter also considers seakeeping performance at multiple conditions. A surrogate model is used, based on stochastic radial basis functions with lower confidence bounding, as a supervised active learning approach. Furthermore, a multi-fidelity formulation, leveraging on unsteady Reynolds-averaged Navier–Stokes equations and potential flow solvers, is used in order to reduce the computational cost of the SDDO procedure. Exploring a five-dimensional design space based on free-form deformation under limited computational resources, the optimal configuration achieves a resistance reduction of about 3% at the escape speed and about 6.4% on average over the operational speed range.

Keywords: simulation-driven design; shape optimization; ship hydrodynamics; multi-fidelity; surrogate modeling; supervised learning; active learning; efficient global optimization

check for updates

Citation: Spinosa, E.; Pellegrini, R.; Posa, A.; Broglia, R.; De Biase, M.; Serani, A. Simulation-Driven Design Optimization of a Destroyer-Type Vessel via Multi-Fidelity Supervised Active Learning. *J. Mar. Sci. Eng.* **2023**, *11*, 2232. https://doi.org/10.3390/jmse11122232

Academic Editor: Decheng Wan

Received: 3 October 2023
Revised: 20 November 2023
Accepted: 22 November 2023
Published: 25 November 2023

1. Introduction

In the early 2000s, the International Maritime Organization (IMO) embarked on initiatives to improve vessel energy efficiency and reduce CO_2 emissions from maritime activities. A significant milestone was achieved in 2011 [1] when the IMO enforced the Energy Efficiency Design Index (EEDI) and the Ship Energy Efficiency Management Plan (SEEMP) to promote greenhouse gas reduction in the global maritime sector (effectively enacted in 2013). Finally, in 2023, the focus of the IMO intensified on decarbonization [2], aligning with the 2023 IMO MEPC strategy to comprehensively reduce greenhouse gas emissions from ships.

With the aim of providing new hull forms, empirical methods can be used to assess their performance [3], or simulation-driven design optimization (SDDO) frameworks [4] can provide an enhancement of the entire design process of novel vessels. In the latter case, numerical simulations are coupled with shape modification tools and optimization algorithms in order to automatize and speed up the design process, leveraging on the use of high-fidelity solvers. Nevertheless, SDDO based on high-fidelity solvers only is still extremely expensive in terms of computational cost and does not provide new design solutions within a reasonable time frame, especially if multiple operational and environmental conditions are taken into consideration, or if a multidisciplinary analysis is needed. For this reason, several cost-reduction methods have been developed in recent years in the SDDO context for hull form optimization [5]. Among them, multi-fidelity approaches [6] generally exploit a large number of low-fidelity, less computationally expensive simulations to assess the design space and a small number of high-fidelity, more computationally expensive computations to identify the optimal design. The majority of multi-fidelity approaches are based on supervised learning methods, exploiting surrogate modeling formulations, like Gaussian processes/Kriging [7–9], radial basis functions [10,11], and support vector regression [12,13]. Finally, to further reduce the computational burden associated with the search for the global optimum, efficient global optimization strategies have been developed thanks to the use of adaptive sampling or active learning. Instead of building the surrogate model with a large amount of samples uniformly distributed within the design space, active learning starts with a limited number of samples and iteratively adds new samples just where they are most useful for the optimization process [14,15]. Examples of SDDO procedures based on multi-fidelity supervised learning for marine application are still limited: a multi-fidelity Gaussian process with Bayesian optimization is presented in [16] for the seakeeping optimization of a SWATH model; a co-Kriging technique is used in [17] for the design optimization of a marine propeller, whereas a comparison of its effectiveness with single-fidelity Kriging is shown in [18] for the optimization of the DTMB 5415 model. Furthermore, examples that include active learning processes in the multi-fidelity context for marine applications are even more limited: stochastic radial basis functions are used in combination with adaptive sampling in [15,19] for hydrofoil and destroyer optimization.

Herein the preliminary design optimization of a destroyer-type vessel is carried out under limited computational resources, with the objective of reducing the ratio of total resistance to the ship displacement in calm water at 30 kn (escape/maximum speed) under different operational and geometrical constraints. The geometrical constraints include fixed draft, limited variation of the overall beam, displacement, and length between perpendiculars, and finally a reserved volume for the sonar in the bow dome. The operational constraints are based on the single significant amplitudes of roll and pitch motions, addressing the subsystem seakeeping performance as per NATO STANAG 4154 [20]. It is worth noting that both power requirements and propeller sizing are directly dependent on the performance at escape/maximum speed. This is the reason to conduct a single-point optimization, at least in the preliminary design phase. The optimization is formulated as a constraint single-objective problem for the bare hull with skeg at the model scale. The shape modification is based on the free-form deformation (FFD) method [21], and a design space of five variables is used. The optimization is conducted by using a multi-fidelity supervised learning method, based on an adaptive stochastic radial basis function (SRBF) surrogate model [15,19] and a memetic version of the particle swarm optimization (PSO) algorithm [22]. In-house, high- and low-fidelity solvers are used for the evaluation of the ship resistance in calm water. Specifically, high-fidelity computations are carried out with an unsteady Reynolds-averaged Navier–Stokes (URANS) solver, whereas low-fidelity computations are carried out with a linear potential flow solver. To the authors' best knowledge, this is one of the first examples of the application of a multi-fidelity supervised active learning approach under limited computational resources for marine applications, including geometrical and functional constraints.

The paper is organized as follows: the multi-fidelity supervised active learning method is presented in Section 2; the optimization problem formulation, along with the design space definition and the numerical solver descriptions are given in Section 3; the discussion of the results is in Section 4; and, finally, concluding remarks are addressed in Section 5.

2. Multi-Fidelity Supervised Active Learning Method

Consider the following single-objective optimization problem

$$\begin{aligned} \text{minimize} \quad & f(\mathbf{x}) \\ \text{subject to} \quad & g(\mathbf{x}) \leq 0 \\ \text{and to} \quad & \mathbf{x}_l \leq \mathbf{x} \leq \mathbf{x}_u \end{aligned} \tag{1}$$

where f is the objective function, g is an inequality constraint, and $\mathbf{x} \in \mathbb{R}^D$ is the design variables vector of dimension D, with $\mathbf{x}_l$ and $\mathbf{x}_u$ its lower and upper bounds, respectively.

In the SDDO context, the objective function evaluation via computational fluid dynamics (CFD) simulations can be very expensive. For this reason, instead of solving directly the problem defined in Equation (1), supervised learning methods, such as surrogate modeling, are used to alleviate the computational burden of the overall optimization process, providing an approximation $\widetilde{f}$ of f at a computational cost that is usually orders of magnitude lower than a CFD simulation. Nevertheless, the construction of a surrogate model based only on high-fidelity simulations can still be onerous. For this reason, the use of multi-fidelity approximations $\widehat{f}$ of f facilitates the solution of the problem in Equation (1) even more. Finally, to further reduce the computational burden of the optimization process, the surrogate model can be refined during the optimization process with an active learning method to add information and improve the approximation of the objective function in specific regions of interest of the design space. The same consideration can be made, even for the constraints evaluations. Therefore, the optimization problem in Equation (1) can be recast as follows:

$$\begin{aligned} \text{minimize} \quad & \widehat{f}(\mathbf{x}) \\ \text{subject to} \quad & \widehat{g}(\mathbf{x}) \leq 0 \\ \text{and to} \quad & \mathbf{x}_l \leq \mathbf{x} \leq \mathbf{x}_u \end{aligned} \tag{2}$$

The following subsections present the supervised learning, the multi-fidelity, and the active learning methods.

2.1. Supervised Learning Method

The supervised learning approach for the approximation of a generic function, denoted as q, relies on SRBF surrogate modeling as discussed in [23]. The process involves a training dataset $\mathcal{T}$ comprising pairs of input variables $\mathbf{x'}_i$ and corresponding function values $q(\mathbf{x'}_i)$, where i ranges from 1 to J. The input variables are standardized to a unit hypercube, and the RBF prediction is determined using a power function kernel. This prediction is defined by:

$$h(\mathbf{x}, \tau) = \mathbb{E}[\mathbf{q}] + \sum_{j=1}^{K} w_j |\mathbf{x} - \mathbf{c}_j|^{\tau}. \tag{3}$$

Here, $\mathbb{E}$ is the expected value, w_j represents the unknown coefficients, $\mathbf{c}_j$ denotes the RBF centers (comprising K points), and τ is a stochastic tuning parameter sampled from a uniform distribution within the range from $\tau_{\min} = 1$ (polyharmonic spline with linear kernel, [24]) to $\tau_{\max} = 3$ (polyharmonic spline with cubic kernel, [25]). Notably, the choice of the distribution for τ is arbitrary and serves as a representation of the degree of belief in the tuning parameter.

The SRBF surrogate model, denoted as $\widetilde{h}(\mathbf{x})$, is computed by approximating the expected value of h over τ using the Monte Carlo method as described in [26]. This approximation is expressed as:

$$q(\mathbf{x}) \approx \widetilde{h}(\mathbf{x}) = \mathbb{E}_{\tau}[h(\mathbf{x}, \tau)] \approx \frac{1}{\Theta} \sum_{i=1}^{\Theta} h(\mathbf{x}, \tau_i). \tag{4}$$

Here, Θ represents the number of samples for τ, set to 100 in this context. The study imposes the exact interpolation of the training set by setting $K = J$. The coefficients w_j are computed by solving the equation:

$$\mathbf{A}\mathbf{w} = (\mathbf{q} - \mathbb{E}[\mathbf{q}]) \tag{5}$$

with $\mathbf{w} = [w_1, \ldots, w_J]^{\mathsf{T}}$, $\mathbf{A}_{ij} = ||\mathbf{x}_i - \mathbf{c}_j||^{\tau}$ with $\mathbf{c}_j = \mathbf{x}'_j$, and $\mathbf{q} = [q(\mathbf{x}'_1), \ldots, q(\mathbf{x}'_J)]^{\mathsf{T}}$.

The uncertainty associated with the SRBF surrogate model prediction, denoted as $U_{\widetilde{h}}(\mathbf{x})$, is quantified using the 95%-confidence band of the cumulative density function (CDF) of $h(\mathbf{x},\tau)$ with respect to τ for a fixed $\mathbf{x}$. The expression for $U_{\widetilde{h}}$ is as follows:

$$U_{\widetilde{h}}(\mathbf{x}) = \mathrm{CDF}^{-1}(0.975;\mathbf{x}) - \mathrm{CDF}^{-1}(0.025;\mathbf{x}), \tag{6}$$

with

$$\mathrm{CDF}(\lambda;\mathbf{x}) \approx \frac{1}{\Theta}\sum_{i=1}^{\Theta} \mathcal{H}[\lambda - h(\mathbf{x},\tau_i)], \tag{7}$$

where $\mathcal{H}(\cdot)$ is the Heaviside step function [23].

Finally, since the SRBF with power kernel has low accuracy when extrapolating, both the surrogate model prediction and the associated uncertainty are bounded (in the following denoted with the subscript 'b'). Specifically, when only one training point is available ($J = 1$), the surrogate model prediction and the associated uncertainty are set equal to the function value at the training point $q(\mathbf{x}')$ as follows:

$$\begin{aligned} \widetilde{h}_b(\mathbf{x}) &= q(\mathbf{x}'_i) \\ U_{\widetilde{h}_b}(\mathbf{x}) &= q(\mathbf{x}'_i) \end{aligned} \tag{8}$$

This approach is consistent with Equation (4), where the expected value of the training set is added to the RBFs, thus providing non-zero prediction when only one training point is available.

On the contrary, when $J > 1$ training points are available, the surrogate model prediction and the associated uncertainty are bounded only in the regions of the domain far from these training points, as follows:

$$\begin{aligned} \widetilde{h}_b(\mathbf{x}) &= \widetilde{h}(\mathbf{x})[1-\sigma(r)] + \mathbb{E}[\mathbf{q}]\sigma(r) \\ U_{\widetilde{h}_b}(\mathbf{x}) &= \min\left(U_{\widetilde{h}}, \mathbb{E}[\mathbf{q}]\right) \end{aligned} \tag{9}$$

with σ, a sigmoid-like function, used to provide a smooth transition between the SRBF prediction and the bounded prediction. Specifically, defining $\mathcal{R}$ as the smallest hyper-rectangle containing the training point coordinates $\{\mathbf{x}'\}_{i=1}^{J}$, whose edges are parallel to the Cartesian axis, the sigmoid-like function is defined as follows:

$$\sigma(r) = \frac{1}{1+\exp[v(r-\gamma)]}, \tag{10}$$

where

$$v = \frac{\alpha}{d_b + \epsilon} \quad \text{and} \quad \gamma = \beta(d_b + \epsilon), \tag{11}$$

r is the Euclidean distance of $\mathbf{x}$ from the $\mathcal{R}$ boundaries, and d_b is the Euclidean distance between the design variable boundaries and the boundary of $\mathcal{R}$.

2.2. Multi-Fidelity Method

Extending the definition of the training set to an arbitrary number L of fidelity levels as $\{\mathcal{T}_k\}_{k=1}^{L}$, with each $\mathcal{T}_k = \{(\mathbf{x}'_j, q_k(\mathbf{x}'_j))\}_{j=1}^{J_k}$, the multi-fidelity approximation $\widehat{h}_k(\mathbf{x})$ of $q(\mathbf{x})$ reads [27]

$$\widehat{h}_k(\mathbf{x}) := \widetilde{h}_L(\mathbf{x}) + \sum_{i=k}^{L-1} \widetilde{\varepsilon}_i(\mathbf{x}), \tag{12}$$

where $\widetilde{h}_L$ is the single-fidelity surrogate model associated with the lowest-fidelity training set (constructed as in Equation (4)), and $\varepsilon_i(\mathbf{x})$ is the inter-level error surrogate with the associated training set $\mathcal{E}_i = \{(\mathbf{y}, \phi - \widehat{h}_i(\mathbf{y})) \mid (\mathbf{y}, \phi) \in \mathcal{T}_{i-1}\}$.

Assuming that the uncertainty associated with the prediction of the lowest-fidelity $U_{\widetilde{h}_L}$ and the inter-level errors $U_{\widetilde{\varepsilon}_i}$ are uncorrelated, the multi-fidelity approximation $\widehat{h}(\mathbf{x})$ of $q(\mathbf{x})$ and its uncertainty $U_{\widehat{h}}$ read

$$q(\mathbf{x}) \approx \widehat{h}(\mathbf{x}) = \widetilde{h}_L(\mathbf{x}) + \sum_{i=1}^{L-1} \widetilde{\varepsilon}_i(\mathbf{x}) \tag{13}$$

$$U_{\widehat{h}}(\mathbf{x}) = \sqrt{U^2_{\widetilde{h}_L}(\mathbf{x}) + \sum_{i=1}^{L-1} U^2_{\widetilde{\varepsilon}_i}(\mathbf{x})}. \tag{14}$$

2.3. Active Learning Method

The multi-fidelity surrogate model is dynamically updated by adding new training points. A new training point $\mathbf{x}^\star$ is identified based on an acquisition function $\psi(\mathbf{x})$, here defined by the lower confidence bounding (LCB) criterion [28], which aims to find points with large prediction uncertainty and small objective function values. Accordingly, LCB-based sampling strategies identify a new training point by solving the following minimization problem:

$$\begin{aligned} \text{minimize} \quad & \psi(\mathbf{x}) = \alpha\widehat{h}(\mathbf{x}) - (1-\alpha)U_{\widehat{h}}(\mathbf{x}) \\ \text{subject to} \quad & \widehat{g}(\mathbf{x}) \leq 0 \\ \text{and to} \quad & d_{\mathcal{T}}(\mathbf{x}) \geq d_0 \\ \text{and to} \quad & \mathbf{x}_l \leq \mathbf{x} \leq \mathbf{x}_u, \end{aligned} \tag{15}$$

where $d_{\mathcal{T}}$ is the minimum distance from the existing training sets, which has to be greater than the threshold value d_0 (minimum acceptable distance to an existing training point) to prevent ill-conditioning problems for the matrix $\mathbf{A}$ in Equation (5) and the occurrence of new sampling points too close to the previous ones. The coefficient α in Equation (15), which is utilized in the formulation of the acquisition function ψ, plays a pivotal role in striking a balance between exploration and exploitation within the design space. When α is set to 1, the acquisition function is primarily employed to directly search for the optimum predicted by the surrogate model. However, this approach may not yield effective results, particularly during the initial stages of the training process when the accuracy of the response surface is often significantly compromised due to the limited number of sampled data points. In contrast, when α is set to 0, the acquisition function is utilized to identify regions of maximum uncertainty in the prediction. This strategy is undoubtedly valuable for achieving a robust global approximation of the response surface. Nonetheless, it can be resource intensive and may lead to the exploration of areas within the design space that are not relevant from an optimization perspective. To strike a balanced approach that encompasses both exploration and exploitation, a common choice is to set $\alpha = 0.5$, which coincides with the standard formulation of the LCB method.

Once $\mathbf{x}^\star$ is identified, to automatically select the fidelity level to sample, a fidelity selection vector $\boldsymbol{\varphi}$ is defined as follows:

$$\boldsymbol{\varphi} \equiv \{U_{\widetilde{\varepsilon}_1}/\beta_1, ..., U_{\widetilde{\varepsilon}_{L-1}}/\beta_{L-1}, U_{\widetilde{f}_L}/\beta_L\}, \tag{16}$$

where $\beta_i = c_i/c_1$, $i = 1, ..., L$, with c_i as the computational cost associated with the i-th level. Using a non-nested training set, the i-fidelity level to sample is defined by identifying the maximum value in $\boldsymbol{\varphi}$ as follows:

$$k = \text{maxloc}(\boldsymbol{\varphi}) \quad \text{with} \quad i = k \tag{17}$$

Finally, Figure 1 shows the extended design structure matrix (XDSM, [29]) of the overall supervised active learning for multi-fidelity surrogate-based shape optimization with limited available budget. Note that the scheme is shown for a two-fidelity procedure, as in the present work, and consequently, the NCC is the normalized computational cost, where the high-fidelity evaluations have a cost equal to 1 and the low-fidelity ones have a cost equal to β.

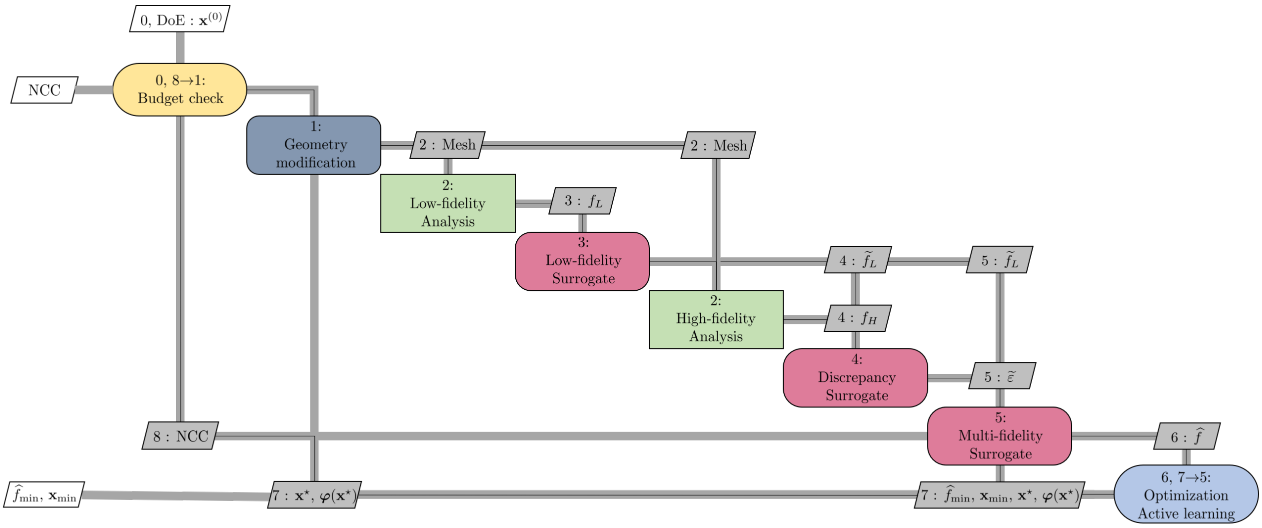

Figure 1. XDSM diagram of the supervised active learning workflow for multi-fidelity surrogate-based shape optimization with two fidelity levels and budget-limited computational costs.

3. Optimization Problem Formulation and Setup

The hull under investigation is a destroyer-type vessel. Specifically, the bare hull with skeg only (see Figure 2) is the subject of the optimization problem. The main parent hull details are listed in Table 1, where T is the ship draft, L_{pp} is the length between perpendiculars, ∇ is the displacement, and B_{OA} the overall beam.

Figure 2. Side view of the original destroyer-type hull (red) with the skeg (orange). The blue line indicates the undisturbed water level.

Table 1. Main non-dimensional parameters of the model scale ($\lambda = 1/28$) parent hull.

Parameter	Symbol	Value	Units
Displacement	∇	0.4660	tonnes
Length between perpendiculars	L_{pp}	5.9643	m
Beam overall	B_{OA}	0.8679	m
Draft	T	0.2046	m

The single-objective problem reads

$$
\begin{aligned}
\text{minimize} \quad & R/\nabla(\mathbf{x}) \\
\text{subject to} \quad & \Omega(\mathbf{x}) > 90\%, \\
& T(\mathbf{x}) = T_0, \\
\text{and to} \quad & \gamma_l \leq \left(L_{\text{pp}}(\mathbf{x})/L_{\text{pp},0} - 1\right) \cdot 100 \leq \gamma_u, \\
& \gamma_l \leq \left(\nabla(\mathbf{x})/\nabla_0 - 1\right) \cdot 100 \leq \gamma_u, \\
& \gamma_l \leq \left(B_{\text{OA}}(\mathbf{x})/B_{\text{OA},0} - 1\right) \cdot 100 \leq \gamma_u, \\
& V(\mathbf{x}) \geq V_0, \\
& \mathbf{x}_l \leq \mathbf{x} \leq \mathbf{x}_u
\end{aligned}
\tag{18}
$$

where R is the total resistance in calm water at $\mathrm{Fr} = 0.381$ (30 kn at full scale), Ω is the ship operabiltity, and V is the volume reserved for the sonar in the dome. Subfix '0' denotes the parent hull values, whereas γ_l and γ_u refer to the lower and upper inequality limits as percentages.

Given the general formulation for the optimization, two problems are defined and denoted as A and B:

- **Problem A**: $\gamma_l = 0\%$ and $\gamma_u = +3\%$, admitting only solutions that maintain the original lower dimensions, with the possibility of increasing them only by 3% with respect to the parent hull.
- **Problem B**: $\gamma_l = -3\%$ and $\gamma_u = +3\%$, admitting a maximum variation of $\pm 3\%$ with respect to the parent hull.

The main reason to split the problem into two is to assess the performance of the vessel using (A) quite strict housing and space requirements (related to the beam, length, and displacement), as well as (B) their relaxation. It may be noted that any reduction in resistance due to displacement reduction for problem B is compensated by the objective function definition (ratio of the resistance to the displacement), allowing for a fair comparison of the two problems.

The operability is evaluated as

$$\Omega(\mathbf{x}) = \int_{\mathcal{Y}} \bigcap_{n=1}^{2} [\mathrm{SSA}_n(\mathbf{x}, \mathbf{y}) \leq \mathrm{SSA}_n^{\star}] p(\mathbf{y}) \mathrm{d}\mathbf{y} \tag{19}$$

where $\mathbf{y}$ are the operational conditions. Here, the single significant amplitude (SSA) of the roll and pitch motions (*subsystem seakeeping performance criteria* as per [20]) are considered for 12 kn speed at sea state 6 (significant wave height, $H_{1/3}$ equal to 5 m and modal period, T_p equal to 12.4 s) and 20 kn at sea state 3 ($H_{1/3} = 0.88$ m and $T_p = 7.5$ s), considering the North Atlantic Ocean [30] with a uniform probability distribution for wave headings and sea state, using a Bretschneider spectrum. Roll and pitch maximum SSA values are 8 and 3 deg, respectively.

3.1. Design Space Definition

A different number of active control points, as well as their degrees of freedom and range of variation, were preliminarily investigated, but for the sake of simplicity, only the selected design space is here described in detail. The design space is defined by five variables, corresponding to the degrees of freedom (DoF) of the "active" nodes of the FFD lattice, shown in blue in Figure 3. In particular, the FFD nodes are composed of a $9 \times 3 \times 3$ lattice in x, y, and z-layer directions, respectively. The five active nodes have only one DoF, which corresponds to the design variables as detailed in Table 2. Finally, Figure 3 (bottom) provides also the shape modification associated with the minimum and maximum value of each design variable. FFD is based on the Bernstein polynomial and the active control points, their degrees of freedom, and the associated range of variation are defined in order to avoid unfeasible designs, allowing for the smooth and fair deformation of the hull embedded by the FFD lattice. For the specific details of the FFD method, the reader can refer to [31].

Table 2. Definition of the design variables in the FFD domain.

Variable	x-Layer	y-Layer	z-Layer	DoF	x_l	x_u
x_1	1	2	1	y	−0.500	0.500
x_2	1	2	2	y	−0.500	0.500
x_3	2	2	1	y	−0.500	0.500
x_4	9	2	1	x	−0.100	0.000
x_5	9	2	2	x	−0.100	0.100

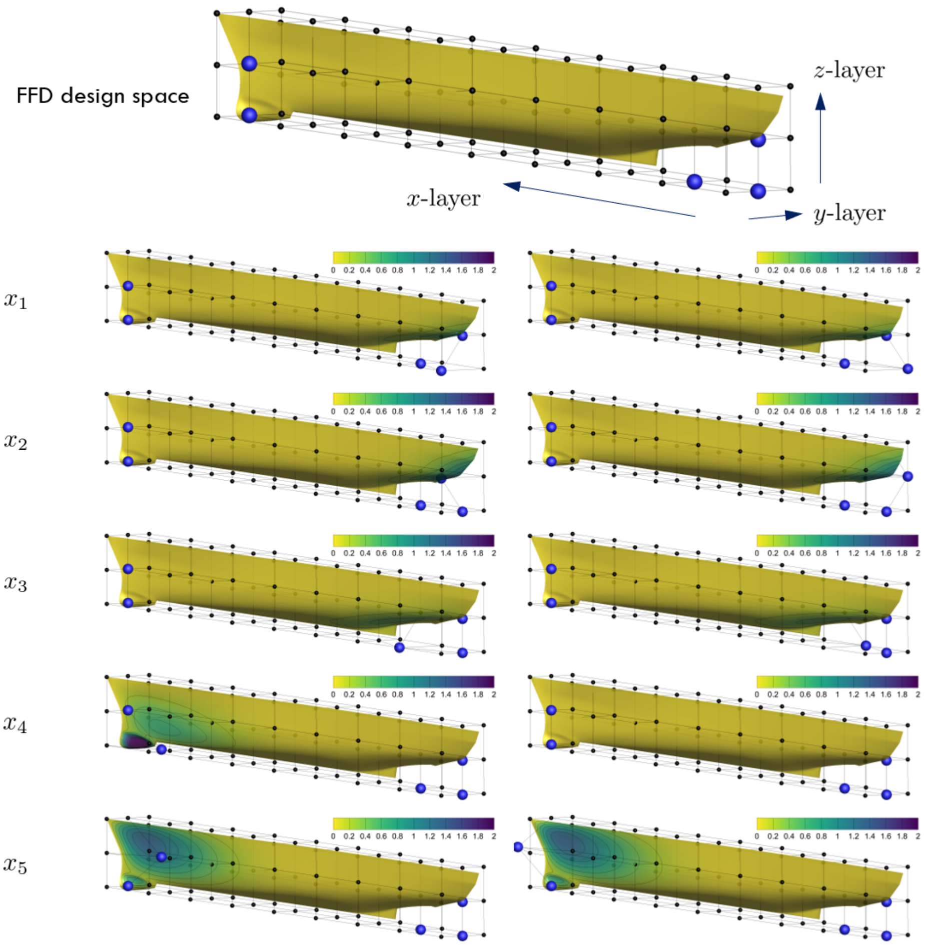

Figure 3. FFD design space: (**top**) lattice with active nodes in blue on top and definition of layer directions; (**bottom**) shape modification associated with minimum and maximum design variables values.

3.2. Numerical Solvers

Multi-fidelity surrogate-based optimization leverages multiple information sources. Specifically, the calm-water total resistance evaluation is based on both high- (RANS) and low-fidelity (potential flow) solvers, whereas the estimation of the operability is based on a single-fidelity (strip theory) model. All the simulations are performed using the following conditions: water density $\rho = 998.5\ \mathrm{kg/m^3}$, kinematic viscosity $\nu = 1.09 \times 10^{-6}\ \mathrm{m^2/s}$, and gravity acceleration $g = 9.8033\ \mathrm{m/s^2}$.

3.2.1. URANS Solver

The high-fidelity solver used for the evaluation of the ship resistance in calm water is χnavis, an in-house code, developed at CNR-INM [32]. χnavis is based on a finite-volume discretization of the URANS equations, where the flow variables are defined at the cells centers. Turbulent stresses are modeled through the Boussinesq hypothesis. The turbulent viscosity is computed using the Spalart–Allmaras turbulence model [33]. No wall functions are used, so the computational grids are designed to have the first grid elements off the wall to meet the $y^+ \leq 1$ condition. Free-surface effects are modeled using a single-phase level-set approach [34].

The computational domain extends from $1.5L_{\mathrm{pp}}$ ahead of the hull up to $2.5L_{\mathrm{pp}}$ behind it, $2L_{\mathrm{pp}}$ laterally, and $2L_{\mathrm{pp}}$ vertically. On the solid walls, the velocity is set to zero, and so is the pressure gradient. At the inlet, the velocity is set to its free-stream value, which corresponds to the nominal hull speed, and the pressure is extrapolated from the inside. At the outlet, the pressure is set to zero, whereas the velocity is extrapolated from the inside. On the top boundary, which is always in the air, all the flow variables are extrapolated from the inside. Given the symmetry of the problem with respect to the plane $y = 0$, the solution is computed on the half-hull, with symmetry conditions imposed on the longitudinal plane. The computational grid is composed of 32 blocks, which can be partially overlapped by exploiting the Chimera capabilities [35]. The mesh around the hull is an O-O type, whereas the one around the skeg, which is generated separately, has an O-C topology. For the background, a Cartesian mesh is adopted. The final grid consists of five million volumes and is assembled by an overset pre-processor. The numerical solution is obtained through a multi-grid approach [36], with four grid levels (from the coarsest G4 to the finest G1), with a coarsening ratio of two along each of the curvilinear coordinates. The total number of volumes for the four grids is equal to 5 M, 630 k, 78.3 k, and 9.8 k, from G1 to G4. A detail of the grid G1 around the bulbous bow is shown in Figure 4a.

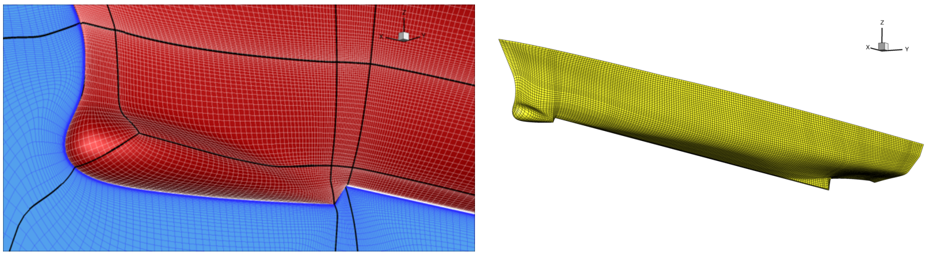

(**a**) χ-navis (**b**) WARP

Figure 4. Details of the computational grids.

The numerical solution is based on a succession of steady states. In particular, the first step is the "even keel" condition (i.e., at a null trim angle and nominal sinkage). The derivatives of the vertical force and pitch moment are estimated by numerical solutions, by a slight perturbation of the trim angle and drift, relative to their initial values. Then, using an iterative procedure, new trim and sinkage are derived by imposing a null pitching moment and the vertical force equal to the ship weight. The procedure goes on until convergence is achieved. Such an approach has a lower computational cost, about 25% lower than a fully unsteady simulation.

3.2.2. Potential Flow Solver

The low-fidelity solver used for the evaluation of the ship resistance in calm water is the WAve Resistance Program (WARP), an in-house code developed at CNR-INM [37].

The total resistance is estimated as the sum of the wave and the skin friction components. The wave resistance is based on a double-model linearization (Dawson's method [38]) and is computed as the integral of pressure over the wetted surface. The skin friction resistance is estimated using a flat plate analogy, based on the local Reynolds number [39]. The equilibrium of the two degrees of freedom for the ship advancing in calm water (sinkage and trim) is reached by means of an iterative procedure, which takes into account the flow equations and the rigid-body dynamics.

The simulations are also in this case performed on the half hull, taking advantage of the problem symmetry. The surface grid counts 200 $\times$ 50 nodes. The computational domain for the free surface extends from $2L_{\mathrm{pp}}$ behind the hull to $1L_{\mathrm{pp}}$ ahead and is $1L_{\mathrm{pp}}$ wide, counting up to 150 $\times$ 50 nodes. Overall, the computational grid counts 17.5 k nodes. The grid is shown in Figure 4b.

WARP is used both for the preliminary assessment of the design space and for the training of the multi-fidelity surrogate model.

3.2.3. Strip Theory Solver

The seakeeping performance is evaluated by a potential flow solution based on the linearized strip theory. The 6DoF response of the ship is provided, advancing at a constant forward speed with arbitrary heading in both regular waves and irregular seas. In addition, the longitudinal, lateral, and vertical responses at specified locations of the ship are also provided.

The hull with the skeg is discretized with 31 computational strips with 10 uniformly distributed nodes along each strip curvilinear coordinate.

4. Results

In the following subsections, the hydrodynamic analysis of the parent hull in calm water is performed using both the low-fidelity and the high-fidelity solvers. A sensitivity analysis of the resistance as a function of the design variables is also carried out. Finally, the results of the optimization and the operability analysis are discussed.

4.1. Preliminary Analysis of the Parent Hull in Calm Water

Figure 5 shows the total resistance, the sinkage, and the trim of the parent hull at model scale at Froude numbers spanning an interval between 0.154 and 0.381, obtained with WARP and χnavis. It should be clarified that the choice of conducting the optimization campaign at model scale is twofold: (i) even if full-scale simulations would be more realistic, they would be more computationally demanding to meet the resolution requirements within the boundary layer ($y^+ \leq 1$, meaning a higher number of cells would be required), otherwise, wall functions need to be used at the expense of accuracy in the evaluation of the frictional component of the forces, especially if large shape modifications are involved; (ii) an experimental campaign at model scale in the CNR-INM towing tank will be conducted in the future for validation of the numerical results.

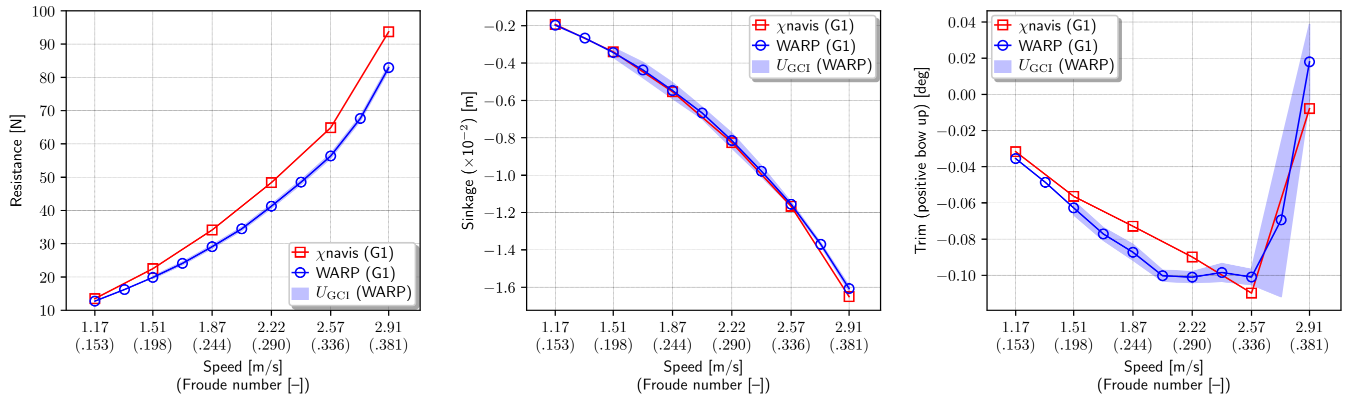

Figure 5. Resistance, sinkage, and trim obtained with the high-fidelity and low-fidelity solvers as a function of the ship speed/Froude number. The uncertainty in the WARP results is also shown as the shaded areas.

The results obtained with the low- and high-fidelity solvers are consistent, although some discrepancies are observed, especially for the resistance values. The potential flow solver underestimates the resistance value with an absolute error, relative to RANS computations, ranging from 4.4% to 9.6%. The discrepancy between the results of the two methods grows at higher speeds, and this can be attributed to the increase in the viscous effects, which the potential flow solver cannot capture. Nevertheless, the low-fidelity solver is appropriate for the purposes defined in Section 3.2.2 because its computational cost is much lower (by about three orders of magnitude) than the high-fidelity one.

It is important to assess the grid uncertainty for WARP and χnavis. In particular, the uncertainty for WARP as a function of the Froude number is plotted as a shaded area in Figure 5, using the GCI method [40]. It is found that grid convergence is reached and that the mean grid uncertainty is below 1% for both the sinkage and the resistance. For the trim angle, the uncertainty is higher, and it is not possible to establish a grid convergence. The reason is that the trim values are very small and close to zero, leading to numerical issues. As far as χnavis is concerned, the grid convergence and the uncertainty analysis are performed only at the highest Froude number under investigation, i.e., Fr = 0.381, using the so-called Factor of Safety method [40]. The results are shown in Table 3.

Table 3. Grid convergence results with χnavis at Fr = 0.381.

	G3	**G2**	**G1**	p	U_{SN}**%G1**
R [N]	131.07	100.64	93.25	2.04	2.64
Sinkage/L_{PP} [–]	-2.440×10^{-3}	-2.730×10^{-3}	-2.777×10^{-3}	2.63	2.20
Trim [deg]	2.073×10^{-3}	4.342×10^{-3}	-1.988×10^{-2}	–	–

The order of accuracy p is close to the expected value of 2. Grid convergence is achieved with a mean uncertainty of about 2.6% and 2.2% for the resistance and the sinkage, respectively. In contrast, the trim angle is oscillatory divergent, and the numerical uncertainty cannot be estimated in these conditions. As per the potential flow solution, this is due to the negligible values of the trim angle. Finally, even if experimental data are not yet available for validation purposes, both potential and viscous solvers have been validated in the past on similar ships with topologically similar computational grids (see [5,41]). Figure 6 shows the pressure coefficient C_p on the hull-wetted surface and the wave pattern. On the free surface, the color map refers to the wave elevation with respect to the undisturbed water level.

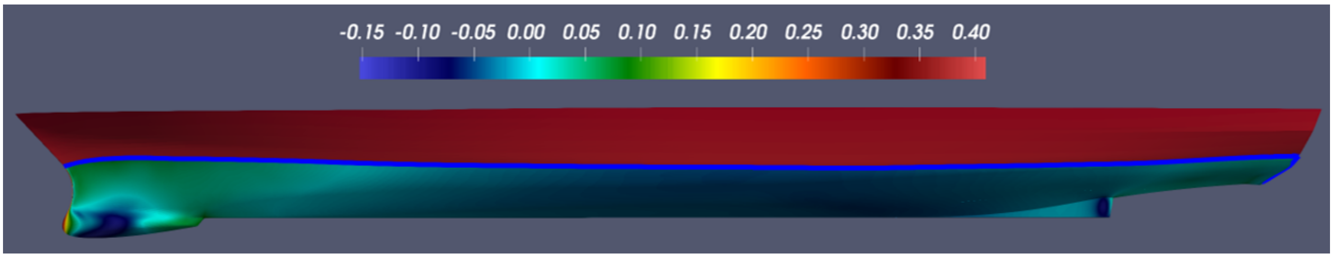

(**a**) Lateral view of the surface pressure coefficient and wave profile (blue line)

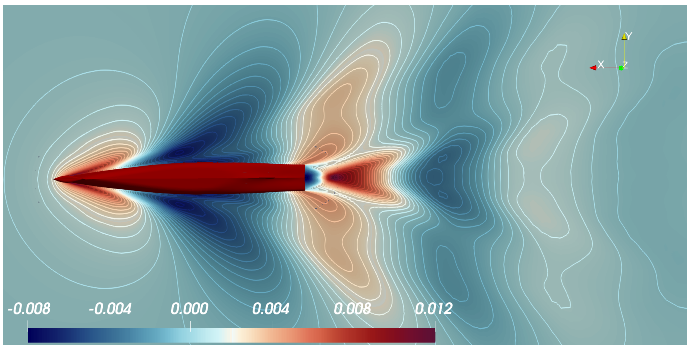

(**b**) Wave elevation view from below

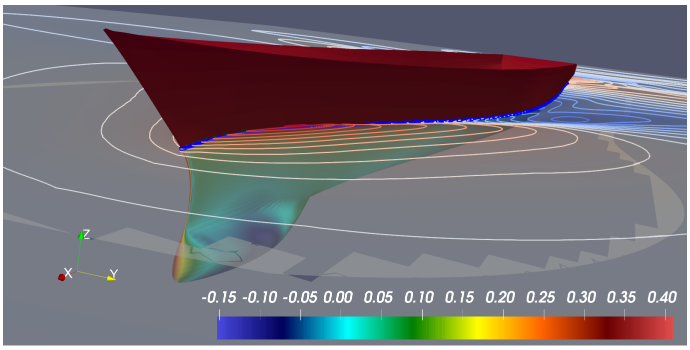

(**c**) Wave elevation and pressure field: 3D view

Figure 6. Contour maps of the pressure coefficient on the wetted surface of the parent hull and of the elevation relative to the undisturbed water level, using the URANS solver.

Finally, using the low-fidelity solver, a sensitivity analysis is performed at Fr = 0.381, where the increment of resistance is evaluated as a function of each single design variable, keeping all the others at their nominal value. The results are shown in Figure 7. The variables are scaled, dividing their value by the corresponding total range of variation. It is demonstrated that by increasing or decreasing each isolated design variable, a reduction of resistance up to 2% can be obtained. With these results, it is possible that an even more significant resistance reduction could be obtained with an appropriate combination of the design variables, at least using the potential flow.

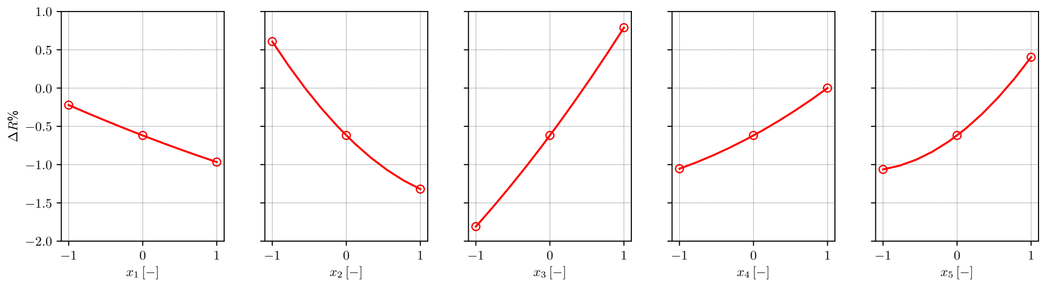

Figure 7. Sensitivity analysis with WARP at Fr = 0.381: variation of the total resistance as a function of the variation of the design variables.

4.2. Shape Optimization Problem

A hybrid global/local version [22] of the deterministic PSO algorithm [42] is used for both the active learning procedure (see Equation (15)) and the solution of the surrogate-based optimization problem (see Equations (2) and (18)). The active learning procedure started with a design of experiment (DoE), based on a face-centered central composite design for the potential flow solution (corresponding to 11 low-fidelity training points, given by the sensitivity analysis, as in Figure 7) and only one high-fidelity training point in the domain center, given by the RANS solver. The training process is limited by a maximum NCC $= 15$, with a computational cost ratio between low- and high-fidelity computations corresponding to $\beta = 0.001$.

Figure 8 shows the convergence of the active learning process in terms of the surrogate prediction of the resistance (top) and associated uncertainty (center), as well as the number of training points for both fidelity levels (bottom). The training process is converged within the limited budget by using 203 low-fidelity simulations and 14 high-fidelity simulations and achieving an uncertainty associated with the resistance prediction at the minimum lower than 0.1% of the training set range. It can be noticed that the training procedures yield a proportional number of high- and low-fidelity samples up to NCC $= 12$, and both the resistance prediction at the minimum and the associated uncertainty are still oscillating. Afterward, the uncertainty decreases rapidly, converging below 0.1%, and the resistance also converges, while the active learning process has mainly requested low-fidelity samples, to just locally refine the surrogate response surface. Once the training process is finished, the optimal solutions for problems A and B are identified and validated with a prediction error $\leq$ 1% relative to RANS computations. The surrogate uncertainty at the minimum and the validation error are two metrics that qualify and quantify the robustness and effectiveness of the proposed active learning procedure. The solution of optimization problems A and B leads to an improvement of the objective function at Fr = 0.381 of 0.9% e 0.3%, respectively. The improvement is not particularly significant, likely because the original ship design at Fr = 0.381 is already well performed. Despite this, considering only the total resistance value, a reasonably good resistance reduction is achieved for problem B (about 3% compared to the parent hull).

Figure 9 shows the variation of the objective function as a function of the Froude number. It is worth noting that, although the variation of the objective function is not significant at the design speed (Fr = 0.381), it is larger at all the other speeds. In particular, in the solution of problem A, the objective function is always higher than the original one, except for the design speed. Considering the speed profile as uniformly distributed, for the sake of simplicity, the average increase is 1.9%, with a peak of 5.3% at Fr = 0.198 (corresponding to 15.6 knots at full scale). On the other hand, the solution of problem B, where the geometrical constraints were allowed to vary between $\pm$3% of their original values, leads to a reduction in the objective function at all speeds, with an average reduction of 3.4%. The maximum reduction of 5.5% occurs at Fr = 0.244 (corresponding to 19.2 knots at full scale). In particular, for problem B, the displacement of the optimal hull lays on the lower bound of the constraint ($-$3%), but this produces beneficial effects for the performance of the vessel in the whole range of speeds. The main geometrical coefficients for the three configurations, the original ones and the optimal ones for problems A and B, are listed in Table 4.

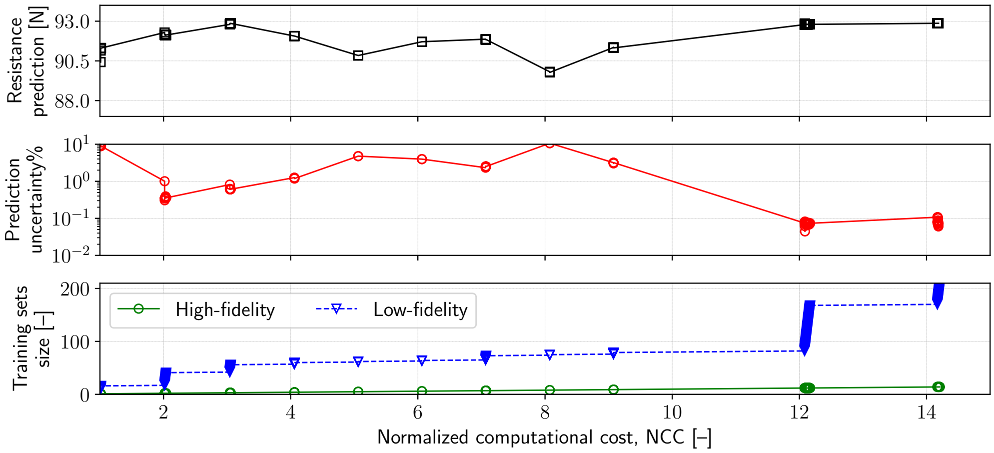

Figure 8. Supervised active learning convergence: convergence of the multi-fidelity surrogate prediction of the resistance (**top**) and associated uncertainty (**center**), and training sets size (**bottom**).

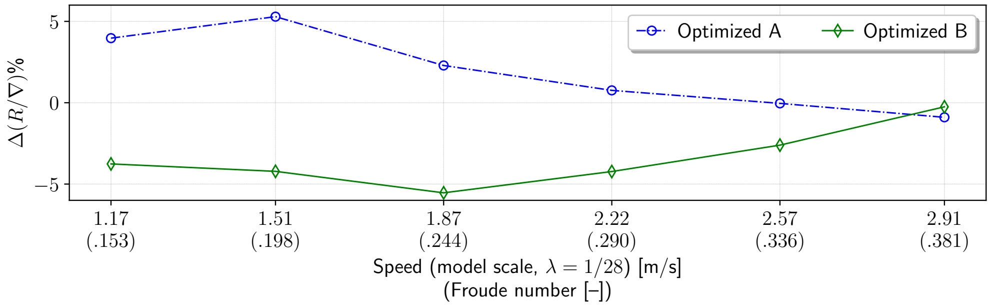

Figure 9. Percentage variation of the objective function as a function of the Froude number, and so the ship speed at model scale.

Table 4. Non-dimensional geometrical coefficients.

Coefficient	Symbol	Original	Optimized A	Optimized B
Block	C_b	0.321	0.321	0.312
Section	C_x	0.516	0.515	0.514
Waterplane	C_{wp}	0.739	0.748	0.719
Prismatic	C_p	0.622	0.624	0.606

Figure 10 shows in the left panels the original (dashed lines) and the optimized (solid lines) hull body plans, and in the right panels the corresponding shape modifications, whereas Figure 11 shows the sectional area diagrams of the original and the two optimized hull shapes. It is observed that both optimized shapes present different sections close to the stern. In particular, the optimized shape A presents a larger transom, whereas shape B has a smaller stern section, a more curved transom and a smaller skeg. Such a geometry is more beneficial for the propeller system since the flow in that region is less disturbed.

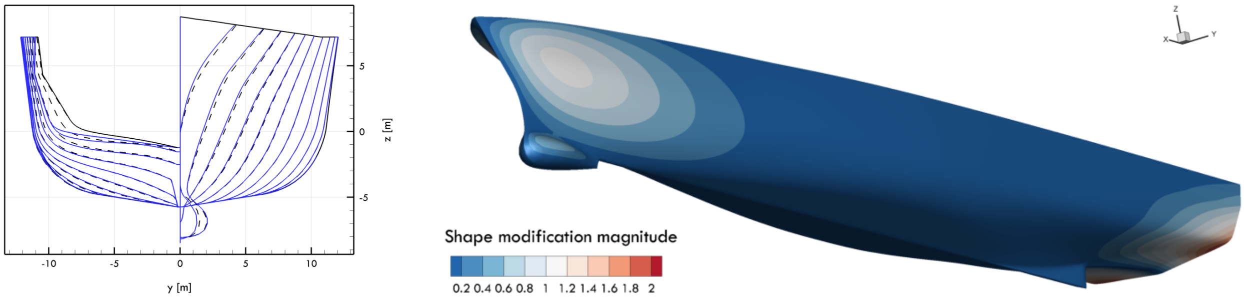

(**a**) Problem A

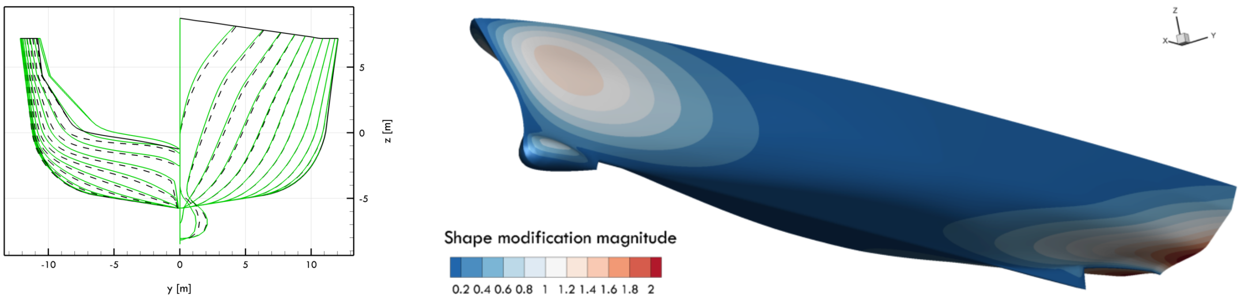

(**b**) Problem B

Figure 10. Comparison between the body plans of the original (black dashed lines) and optimized (colored solid lines) hull shapes derived from the optimization problems A (**top**) and B (**bottom**) on the left; contours of the magnitude of the shape modification from the optimization procedures A (**top**) and B (**bottom**) on the right.

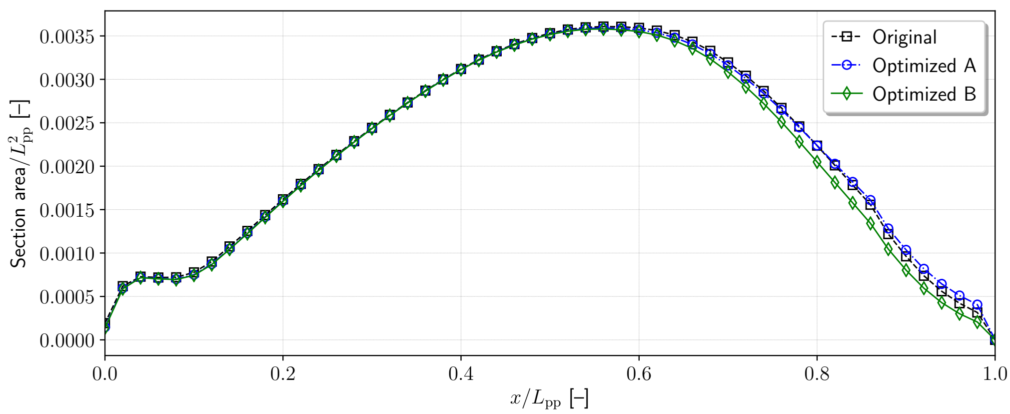

Figure 11. Sectional area diagrams for the original and the optimized hulls: the coordinate 0 corresponds to the bow section, whereas 1 corresponds to the stern.

These differences can be appreciated also in Figure 12, where the pressure fields on the parent hull at Fr = 0.381 are compared with those on the optimized hulls. Details of the bulbous bow and of the skeg are shown in Figure 12a,b, respectively. At the bulbous bow, no significant differences can be observed, whereas there is a pressure reduction at the rear in the region of the skeg. It is also interesting to compare the wave elevation field among the three configurations. This is shown in the contour maps in Figure 13, again at Fr = 0.381. Also in this case, the most significant change between the original and the optimized wave fields can be observed at the rear of the hull.

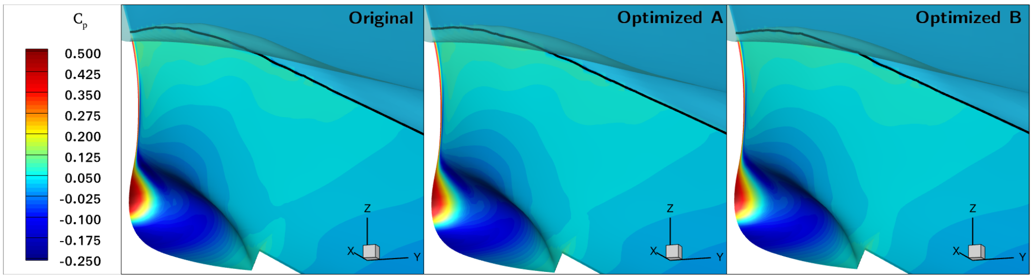

(**a**) Bulbous bow

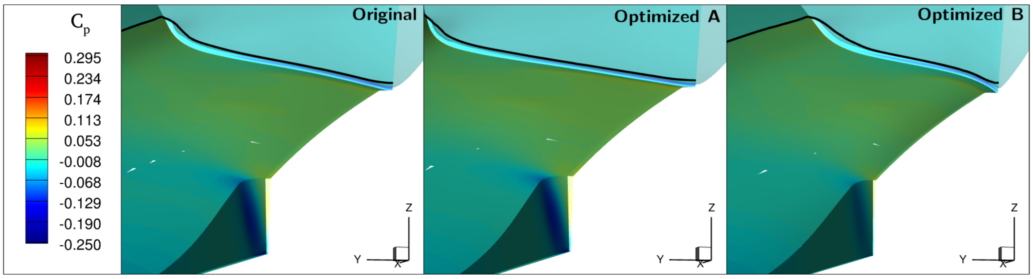

(**b**) Stern and skeg

Figure 12. Contour maps of the pressure coefficient in the bulbous bow region and in the skeg region.

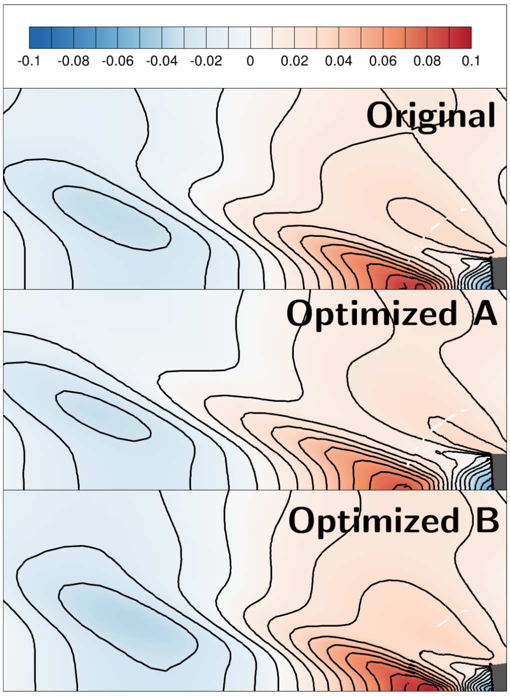

(**a**) Stern

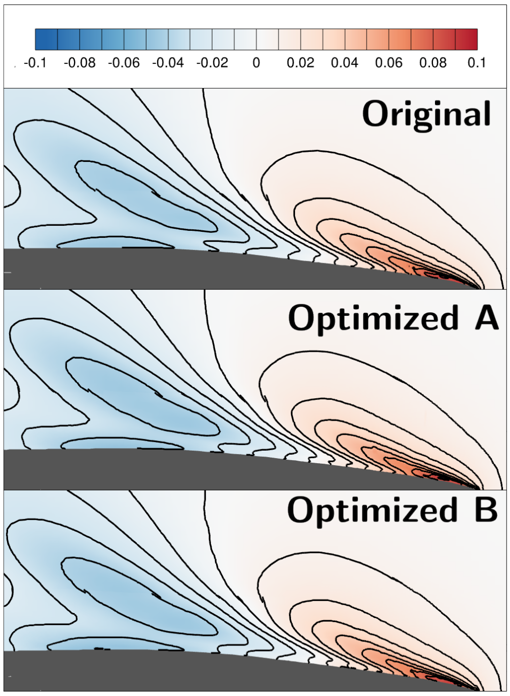

(**b**) Bow

Figure 13. Comparison among the contour maps of the non-dimensional free-surface elevation η/L_{pp} generated by the original and the optimized hulls A and B.

Figure 14 finally provides the resistance, the sinkage, and the trim curves as a function of the ship speed, for the parent and the optimized hulls. It is observed that the resistance curve of the optimized hull B is always below the other ones. The variation of sinkage and trim is not significant.

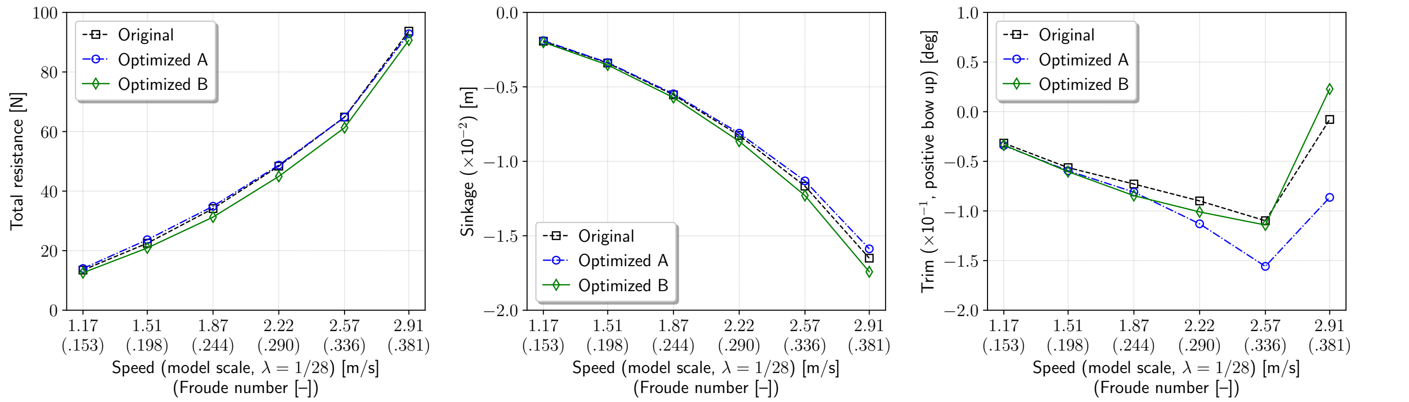

Figure 14. Resistance, sinkage and trim curves: comparison between the parent hull and the optimized hulls.

Finally, Figure 15 shows the operability constraints of the ship. In particular, the RMS of the roll and pitch motions are shown for sea state 3 at 20 kn and sea state 6 at 12 kn. For the pitch motion, all three configurations are within the operability constraint established by the STANAG criterion, see [20]. On the other hand, none of the three configurations meet the requirements for the roll motion (maximum of 8 deg) for heading wave angles between 60 and 150 deg (where 0 deg corresponds to head waves) at sea state 6. Despite this, all three configurations meet the operability condition assigned by the optimization constraints, which is 90%. More specifically, the three hulls have an operability of about 92%.

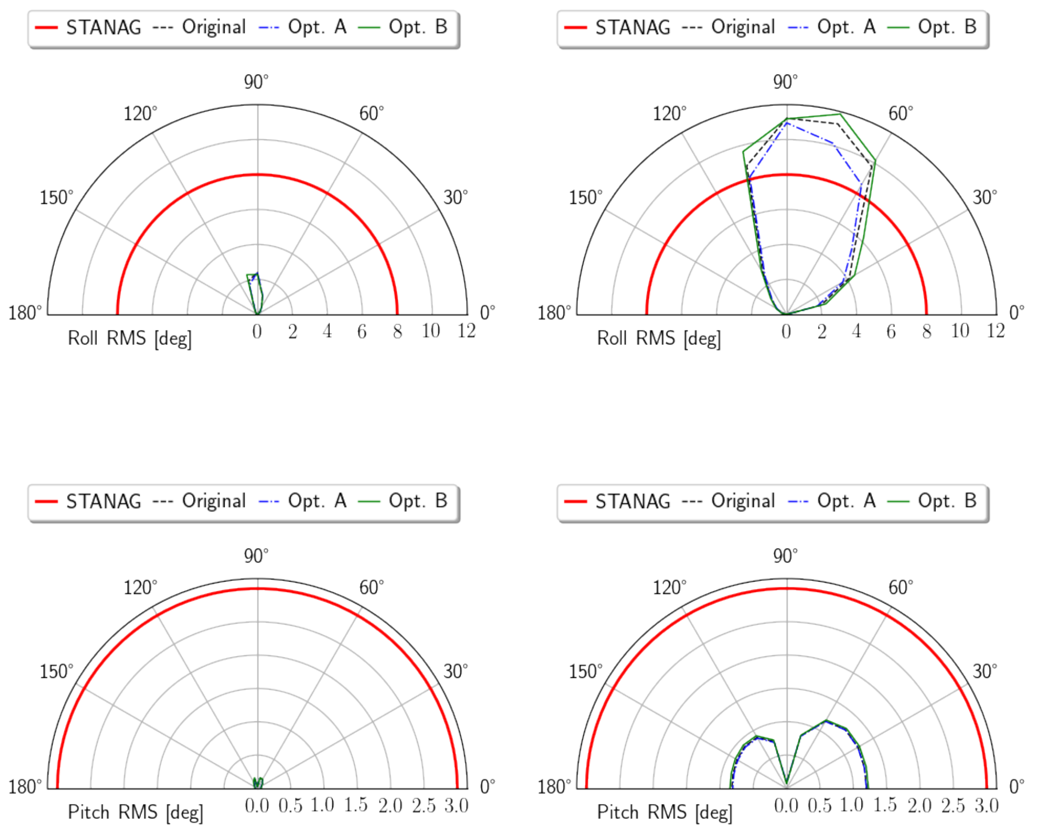

Figure 15. Comparison of the seakeeping performance using SSA of the roll (**top**) and pitch (**bottom**) motions for sea state 3 at 20 kn (**left**) and sea state 6 at 12 kn (**right**).

5. Conclusions and Future Works

This paper presents a simulation-driven design optimization approach based on supervised active learning for the optimization of a destroyer-type vessel, under limited computational resources. The objective function is the resistance over the displacement ratio in calm water at Fr = 0.381. The optimization also takes into account geometrical and operability constraints, related to the seakeeping conditions at sea states 3 and 6. Two optimization problems are solved: A) with geometrical constraints that can only be increased by 3%, and B) with geometrical constraints that can be varied within the range ±3% relative to the original configuration.

A multi-fidelity adaptive surrogate model, based on the stochastic radial basis function, is used to approximate the objective function, exploiting the solution of the hydrodynamic problem using a URANS viscous high-fidelity solver and a low-fidelity potential flow solver. The training process of the surrogate model was very effective since it used 203 low-fidelity solutions and only 14 high-fidelity solutions. Both optimization processes led to a reduction in the objective function lower than 1% at escape speed. This confirms the goodness of the preliminary design. Nevertheless, if the performance of the two optimized hulls are analyzed as a function of the advancement speed, it is observed that the optimized hull B presents a significant performance increase for all the lower speeds in the range under investigation, with a mean resistance reduction of 6.3%, whereas the optimized hull A has reduced performance at lower speeds (1.9% on average). This is an important result that highlights how the design optimization process should not be focused only on one single condition, but for effective results, robust design optimization formulations have to be taken into consideration.

In order to avoid the limitation of deterministic and single-objective formulations, future work will be focused on the development and assessment of supervised active learning approaches capable of taking into consideration both robust optimization formulations and multi-objective problems, as well as multi-fidelity constraints [43]. Furthermore, a possible extension to a dynamic formulation of the lower confidence bounding method, as an acquisition function, will be explored by balancing the weight coefficient with the budget of function evaluation available for the solution of the optimization process. Finally, validation studies will be conducted on both the original and the optimized vessels.

Author Contributions: Conceptualization, R.B., M.D.B. and A.S.; methodology, R.P., R.B. and A.S.; software, R.P., A.P. and R.B.; formal analysis, E.S., R.B. and A.S.; investigation, E.S., R.B. and A.S.; writing—original draft preparation, E.S. and A.S.; writing—review and editing, E.S., R.P., A.P., R.B. and A.S.; visualization, R.B. and A.S.; supervision, R.B., M.D.B. and A.S.; funding acquisition, A.S. All authors have read and agreed to the published version of the manuscript.

Funding: CNR-INM is grateful to the Italian Navy for its support under the 01CT19 contract and acknowledges the support of the Italian Ministry of University and Research (MUR) through the National Recovery and Resilience Plan (PNRR), Sustainable Mobility Center (CNMS), Spoke 3 Waterways, CN00000023—CUP B43C22000440001.

Conflicts of Interest: The authors declare no conflicts of interest. The funders had no role in the design of the study; in the collection, analyses, or interpretation of data; in the writing of the manuscript, or in the decision to publish the results.

References

1. Čampara, L.; Hasanspahić, N.; Vujičić, S. Overview of MARPOL ANNEX VI regulations for prevention of air pollution from marine diesel engines. *SHS Web Conf.* **2018**, *58*, 01004. [CrossRef]
2. IMO. *2023 IMO Strategy on Reduction of GHG Emissions from Ships*; MEPC80/17/Add.1; Annex 15 Resolution MEPC.377(80); IMO: London, UK, 2023.
3. Nikolopoulos, L.; Boulougouris, E. A study on the statistical calibration of the holtrop and mennen approximate power prediction method for full hull form, low froude number vessels. *J. Ship Prod. Des.* **2019**, *35*, 41–68. [CrossRef]
4. Harries, S.; Abt, C. Faster turn-around times for the design and optimization of functional surfaces. *Ocean Eng.* **2019**, *193*, 106470. [CrossRef]

5. Serani, A.; Stern, F.; Campana, E.F.; Diez, M. Hull-form stochastic optimization via computational-cost reduction methods. *Eng. Comput.* **2022**, *38*, 2245–2269. [CrossRef]
6. Beran, P.S.; Bryson, D.; Thelen, A.S.; Diez, M.; Serani, A. Comparison of multi-fidelity approaches for military vehicle design. In Proceedings of the AIAA Aviation 2020 Forum, Virtual Event, 15–19 June 2020; p. 3158.
7. Coppedè, A.; Gaggero, S.; Vernengo, G.; Villa, D. Hydrodynamic shape optimization by high fidelity CFD solver and Gaussian process based response surface method. *Appl. Ocean Res.* **2019**, *90*, 101841. [CrossRef]
8. Miao, A.; Zhao, M.; Wan, D. CFD-based multi-objective optimisation of S60 Catamaran considering Demihull shape and separation. *Appl. Ocean Res.* **2020**, *97*, 102071. [CrossRef]
9. Liu, Z.; Zhao, W.; Wan, D. Resistance and wake distortion optimization of JBC considering ship-propeller interaction. *Ocean Eng.* **2022**, *244*, 110376. [CrossRef]
10. Nazemian, A.; Ghadimi, P. Automated CFD-based optimization of inverted bow shape of a trimaran ship: An applicable and efficient optimization platform. *Sci. Iran.* **2021**, *28*, 2751–2768. [CrossRef]
11. Harries, S.; Uharek, S. Application of radial basis functions for partially-parametric modeling and principal component analysis for faster hydrodynamic optimization of a catamaran. *J. Mar. Sci. Eng.* **2021**, *9*, 1069. [CrossRef]
12. Feng, Y.; Chen, Z.; Dai, Y.; Cui, L.; Zhang, Z.; Wang, P. Multi-objective optimization of a bow thruster based on URANS numerical simulations. *Ocean Eng.* **2022**, *247*, 110784. [CrossRef]
13. Lv, H.; Wei, C.; Liang, X.; Yi, H. Optimisation of wave-piercing trimaran outrigger layout with comprehensive consideration of resistance and seakeeping. *Ocean Eng.* **2022**, *250*, 111050. [CrossRef]
14. Luo, W.; Guo, X.; Dai, J.; Rao, T. Hull optimization of an underwater vehicle based on dynamic surrogate model. *Ocean Eng.* **2021**, *230*, 109050. [CrossRef]
15. Pellegrini, R.; Wackers, J.; Broglia, R.; Serani, A.; Visonneau, M.; Diez, M. A multi-fidelity active learning method for global design optimization problems with noisy evaluations. *Eng. Comput.* **2023**, *39*, 3183–3206. [CrossRef]
16. Bonfiglio, L.; Perdikaris, P.; Vernengo, G.; de Medeiros, J.S.; Karniadakis, G. Improving swath seakeeping performance using multi-fidelity Gaussian process and Bayesian optimization. *J. Ship Res.* **2018**, *62*, 223–240. [CrossRef]
17. Gaggero, S.; Vernengo, G.; Villa, D. A marine propeller design method based on two-fidelity data levels. *Appl. Ocean Res.* **2022**, *123*, 103156. [CrossRef]
18. Liu, X.; Zhao, W.; Wan, D. Multi-fidelity Co-Kriging surrogate model for ship hull form optimization. *Ocean Eng.* **2022**, *243*, 110239. [CrossRef]
19. Wackers, J.; Pellegrini, R.; Serani, A.; Visonneau, M.; Diez, M. Efficient initialization for multi-fidelity surrogate-based optimization. *J. Ocean Eng. Mar. Energy* **2023**, *9*, 291–307. [CrossRef]
20. Kennell, C.G.; White, B.L.; Comstock, E.N. Innovative Naval Designs for North Atlantic Opeartions. *SNAME Trans.* **1985**, *93*, 261–281.
21. Barr, A.H. Global and Local Deformations of Solid Primitives. *SIGGRAPH Comput. Graph.* **1984**, *18*, 21–30. [CrossRef]
22. Serani, A.; Diez, M.; Campana, E.F.; Fasano, G.; Peri, D.; Iemma, U. Globally Convergent Hybridization of Particle Swarm Optimization Using Line Search-Based Derivative-Free Techniques. In *Recent Advances in Swarm Intelligence and Evolutionary Computation*; Studies in Computational Intelligence; Yang, X.S., Ed.; Springer International Publishing: Cham, Switzerland, 2015; Volume 585, pp. 25–47.
23. Volpi, S.; Diez, M.; Gaul, N.; Song, H.; Iemma, U.; Choi, K.K.; Campana, E.F.; Stern, F. Development and validation of a dynamic metamodel based on stochastic radial basis functions and uncertainty quantification. *Struct. Multidiscip. Optim.* **2015**, *51*, 347–368. [CrossRef]
24. Gutmann, H.M. A radial basis function method for global optimization. *J. Glob. Optim.* **2001**, *19*, 201–227. [CrossRef]
25. Forrester, A.I.; Keane, A.J. Recent advances in surrogate-based optimization. *Prog. Aerosp. Sci.* **2009**, *45*, 50–79. [CrossRef]
26. Piazzola, C.; Tamellini, L.; Pellegrini, R.; Broglia, R.; Serani, A.; Diez, M. Comparing multi-index stochastic collocation and multi-fidelity stochastic radial basis functions for forward uncertainty quantification of ship resistance. *Eng. Comput.* **2023**, *39*, 2209–2237. [CrossRef]
27. Serani, A.; Pellegrini, R.; Broglia, R.; Wackers, J.; Visonneau, M.; Diez, M. An adaptive N-fidelity metamodel for design and operational-uncertainty space exploration of complex industrial problems. In Proceedings of the VIII International Conference on Computational Methods in Marine Engineering MARINE, Gothenburg, Sweden, 13–15 May 2019.
28. Serani, A.; Pellegrini, R.; Wackers, J.; Jeanson, C.E.; Queutey, P.; Visonneau, M.; Diez, M. Adaptive multi-fidelity sampling for CFD-based optimisation via radial basis function metamodels. *Int. J. Comput. Fluid Dyn.* **2019**, *33*, 237–255. [CrossRef]
29. Lambe, A.B.; Martins, J.R. Extensions to the design structure matrix for the description of multidisciplinary design, analysis, and optimization processes. *Struct. Multidiscip. Optim.* **2012**, *46*, 273–284. [CrossRef]
30. Bales, S.L. Designing Ships to the Natural Environment. *Nav. Eng. J.* **1983**, *95*, 31–40. [CrossRef]
31. Sederberg, T.W.; Parry, S.R. Free-form deformation of solid geometric models. *ACM SIGGRAPH Comput. Graph.* **1986**, *20*, 151–160. [CrossRef]
32. Di Mascio, A.; Broglia, R.; Muscari, R. Prediction of hydrodynamic coefficients of ship hulls by high-order Godunov-type methods. *J. Mar. Sci. Technol.* **2009**, *14*, 19–29. [CrossRef]
33. Spalart, P.; Allmaras, S. A one-equation turbulence model for aerodynamic flows. In Proceedings of the 30th Aerospace Sciences Meeting and Exhibit, Reno, NV, USA, 6–9 January 1992; p. 439.

34. Broglia, R.; Durante, D. Accurate prediction of complex free surface flow around a high speed craft using a single-phase level set method. *Comput. Mech.* **2018**, *62*, 421–437. [CrossRef]
35. Zaghi, S.; Di Mascio, A.; Broglia, R.; Muscari, R. Application of dynamic overlapping grids to the simulation of the flow around a fully-appended submarine. *Math. Comput. Simul.* **2015**, *116*, 75–88. [CrossRef]
36. Favini, B.; Broglia, R.; Di Mascio, A. Multi–grid Acceleration of Second Order ENO Schemes from Low Subsonic to High Supersonic Flows. *Int. J. Num. Meth. Fluids* **1996**, *23*, 589–606. [CrossRef]
37. Bassanini, P.; Bulgarelli, U.; Campana, E.F.; Lalli, F. The wave resistance problem in a boundary integral formulation. *Surv. Math. Ind.* **1994**, *4*, 151–194.
38. Dawson, C.W. A practical computer method for solving ship-wave problems. In Proceedings of the 2nd International Conference on Numerical Ship Hydrodynamics, Berkeley, CA, USA, 19–21 September 1977; pp. 30–38.
39. Schlichting, H.; Gersten, K. *Boundary-Layer Theory*; Springer: Berlin/Heidelberg, Germany, 2000.
40. Xing, T.; Stern, F. Factors of safety for Richardson extrapolation. *J. Fluids Eng.* **2010**, *132*, 061403. [CrossRef]
41. Serani, A.; Ficini, S.; Broglia, R.; Diez, M.; Goren, O.; Danisman, D.; Solak, H.P.; Yıldız, S.; Nikbay, M.; Scholcz, T.; others. Shape Optimization of a Naval Destroyer by Multi-Fidelity Methods. In Proceedings of the 10th Conference on Computational Methods in Marine Engineering, Madrid, Spain, 27–29 June 2023.
42. Serani, A.; Leotardi, C.; Iemma, U.; Campana, E.F.; Fasano, G.; Diez, M. Parameter selection in synchronous and asynchronous deterministic particle swarm optimization for ship hydrodynamics problems. *Appl. Soft Comput.* **2016**, *49*, 313 – 334. [CrossRef]
43. Rumpfkeil, M.P.; Serani, A.; Beran, P.S. Multi-Fidelity Constrained Optimization Methods Applied to Benchmark Problems. In Proceedings of the 2024 AIAA SciTech Forum, Orlando, FL, USA, 8–12 January 2024 .